Strong-Magnetic-Field Magnon Transport in Monolayer Graphene

Haoxin Zhou,[1,*] Chunli Huang,[2] Nemin Wei,[2] Takashi Taniguchi,[3] Kenji Watanabe,[4] Michael P. Zaletel,[5,6] Zlatko Papić,[7] Allan H. MacDonald,[2] and Andrea F. Young[1,†]

[1]*Department of Physics, University of California at Santa Barbara, Santa Barbara, California 93106, USA*
[2]*Department of Physics, University of Texas at Austin, Austin, Texas 78712, USA*
[3]*International Center for Materials Nanoarchitectonics, National Institute for Materials Science, 1-1 Namiki, Tsukuba 305-0044, Japan*
[4]*Research Center for Functional Materials, National Institute for Materials Science, 1-1 Namiki, Tsukuba 305-0044, Japan*
[5]*Department of Physics, University of California, Berkeley, California 94720, USA*
[6]*Materials Sciences Division, Lawrence Berkeley National Laboratory, Berkeley, California 94720, USA*
[7]*School of Physics and Astronomy, University of Leeds, Leeds LS2 9JT, United Kingdom*

(Received 6 February 2021; revised 22 February 2022; accepted 28 April 2022; published 16 June 2022)

At high magnetic fields, monolayer graphene hosts competing phases distinguished by their breaking of the approximate SU(4) isospin symmetry. Recent experiments have observed an even denominator fractional quantum Hall state thought to be associated with a transition in the underlying isospin order from a spin-singlet charge density wave at low magnetic fields to an antiferromagnet at high magnetic fields, implying that a similar transition must occur at charge neutrality. However, this transition does not generate contrast in typical electrical transport or thermodynamic measurements and no direct evidence for it has been reported, despite theoretical interest arising from its potentially unconventional nature. Here, we measure the transmission of ferromagnetic magnons through the two-dimensional bulk of clean monolayer graphene. Using spin polarized fractional quantum Hall states as a benchmark, we find that magnon transmission is controlled by the detailed properties of the low-momentum spin waves in the intervening Hall fluid, which is highly density dependent. Remarkably, as the system is driven into the antiferromagnetic regime, robust magnon transmission is restored across a wide range of filling factors consistent with Pauli blocking of fractional quantum Hall spin-wave excitations and their replacement by conventional ferromagnetic magnons confined to the minority graphene sublattice. Finally, using devices in which spin waves are launched directly into the insulating charge-neutral bulk, we directly detect the hidden phase transition between bulk insulating charge density wave and a canted antiferromagnetic phase at charge neutrality, completing the experimental map of broken-symmetry phases in monolayer graphene.

DOI: 10.1103/PhysRevX.12.021060

Subject Areas: Condensed Matter Physics, Graphene Magnetism

I. INTRODUCTION

Strongly interacting quantum magnets host a variety of spin- and charge-ordered states. In three-dimensional materials, numerous probes are available that are directly sensitive to spin or charge order, allowing experiment to disambiguate competing states. In two-dimensional van der Waals heterostructures common bulk probes usually have insufficient sensitivity. In their place, experiment typically relies on electrical transport characterization, and on the ability to use electric and magnetic fields to tune microscopic parameters of the Hamiltonian. Comparison with theoretical models can then be used to infer which phases are experimentally realized. Quantum Hall ferromagnetism in graphene provides a paradigmatic experimental example. Here the intrinsic flatness of the Landau level bands makes Coulomb interactions dominant, while the spin and valley degeneracy endow the Landau levels with a multicomponent nature that allows for a large number of competing orders. At charge neutrality, for example, predicted phases include a spin polarized ferromagnet (FM) [1,2], a canted antiferromagnet (CAF) [3–5], a lattice scale charge density wave (CDW), and a partially sublattice polarized (PSP) bond-density wave [5–7]. The variety of competing phases is even more

*Present address: Department of Applied Physics and Materials Science, California Institute of Technology, Pasadena, California 91125, USA.
†andrea@physics.ucsb.edu

abundant at nonzero Landau level fillings [8,9], featuring a subtle interplay of ferromagnetic physics and the correlations underlying the fractional quantum Hall effect. Crucially, the relative favorability of different isospin symmetry breaking phases can be tuned experimentally by varying the charge carrier density, Zeeman energy, and a substrate induced sublattice splitting.

Experiments to date have focused on detection of the FM and CAF spin-ordered states, which are distinguished by edge mode properties that differentiate their two-terminal conductances [10,11]. In most cases, however, phases cannot be distinguished by electrical transport. For example, transport cannot detect the transition at charge neutrality between spin-ordered CAF states and charge-ordered CDW or PSP states, which has attracted theoretical attention as an analog of the Neél to valence bond solid transition studied in models of quantum magnetism [12,13]. This transition is expected to occur [7] in samples with a finite sublattice splitting, which in monolayer graphene can be induced by a hexagonal boron nitride (*h*-BN) substrate [14,15]. In this scenario, a CDW state obtains at low magnetic fields where the sublattice splitting is dominant. As the magnetic field is raised, the strength of the Coulomb interactions grows, including the strength of the short-range interactions that distinguish the valleys and favor the CAF state. Once these are sufficiently large, the CDW gives way to the CAF phase via a partially sublattice polarized phase featuring a Kekulé distortion of the charge density wave order. Experimentally, indirect evidence for this transition has been reported in samples that show a sublattice gap at $B_{\mathrm{tot}} = 0$ [16].

Here, we fabricate two types of gate-defined monolayer graphene lateral junctions which allow electrically actuated magnon transmission measurements [17–19] to directly probe isospin polarization, independent of its influence on charge transport. We use these devices to systematically study the isospin phases in the fractional quantum Hall regime and at the charge neutrality point.

II. MAGNON TRANSMISSION IN THE FRACTIONAL QUANTUM HALL REGIME

The schematic structure and optical micrograph of device A is shown in Fig. 1(a). The monolayer graphene sheet is encapsulated with two hexagonal boron nitride layers. On the top and bottom are two single-crystal graphite gates that are patterned with holes to control different regions of the graphene layer. The heterostructure sits on top of a *p*-doped silicon chip covered by a 285-nm-thick silicon dioxide layer. Applying voltages on the two graphite gates and the silicon gate allows independent control of the carrier density in regions I, II, and III [rendered in white, pink, and blue, respectively, in Fig. 1(a)]. Electrical contacts to the monolayer graphene are made inside two holes, allowing charge transport measurement both along the internal edge and through the bulk separating the two "islands." Figures 1(b)

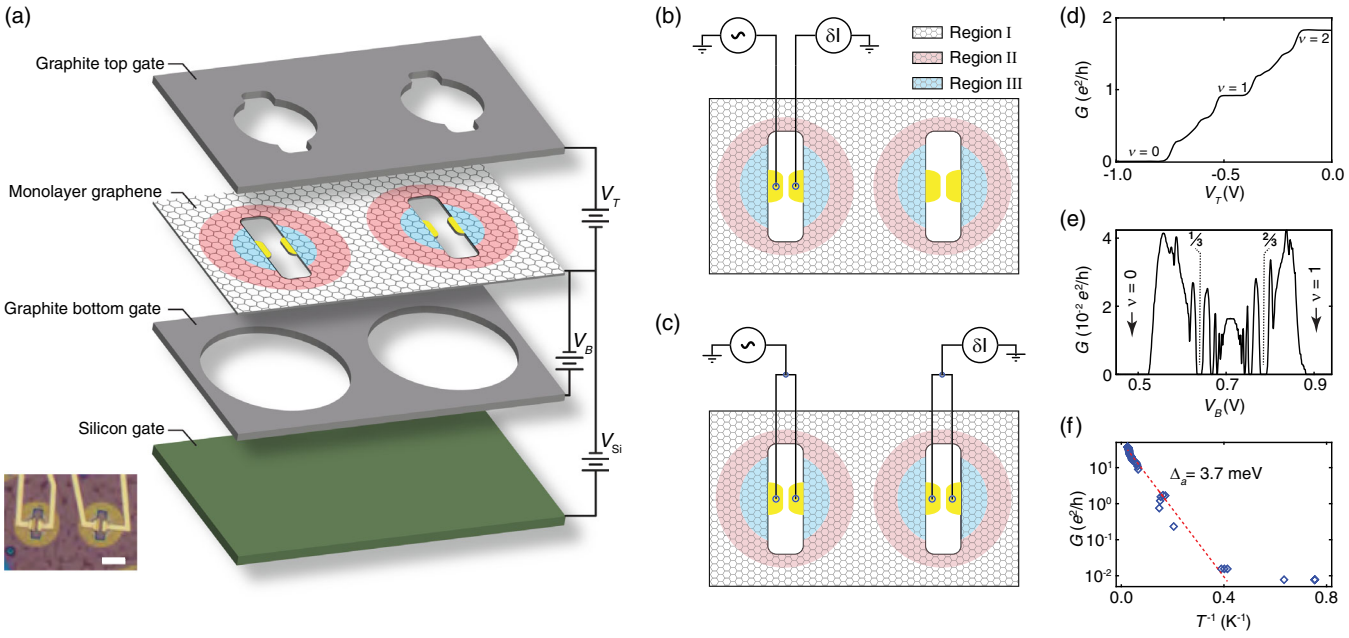

FIG. 1. Transport measurement on device A. (a) Schematic of the device geometry. Inset: optical micrograph of the sample. Scale bar represents 5 μm. (b) Schematic of the intraisland transport measurement. (c) Schematic of the interisland transport measurement. (d) Intraisland conductance as a function of V_T measured at $B_\perp = 8$ T, $V_B = 0$, and $V_{\mathrm{Si}} = 10$ V. V_B, V_T, and V_{Si} are the voltage applied on the graphite top gate, the graphite bottom gate, and the silicon gate, respectively. (e) Interisland conductance as a function of V_B measured at $B_\perp = 8$ T, $V_T = -0.3556$ V, $V_{\mathrm{Si}} = 6.5$ V. (f) Arrhenius plot of the conductance at the charge neutrality point; linear fitting of the data shows the sample is insulating with an energy gap of 3.7 meV.

and 1(c) show the wiring of intraisland charge transport and interisland charge transport measurements, respectively. In the former case, the two electrodes are connected by inner boundaries of the monolayer graphene. The conductance is dominated by edge states in the quantum Hall regime. We use this wiring configuration to tune the carrier densities in regions II and III of the sample to the desired values, which is crucial for the magnon transmission measurements described below. A typical result at $B_\perp = 8$ T is shown in Fig. 1(d). By applying $V_{\mathrm{Si}} = 6.5$ V and $V_B = -0.3556$ V, we can set the Landau level filling factors $\nu_{\mathrm{II}} = 1$, $\nu_{\mathrm{III}} = 2$. For the interisland charge transport measurement, the two electrodes are not coupled by any physical or gate-defined boundaries. The conductance, therefore, is determined by the bulk conductance of the sample. A typical result at $B_\perp = 8$ T is shown in Fig. 1(e), where $B_\perp$ is the perpendicular magnetic field.

Temperature-dependent interisland transport measurement shows that the device features a thermal activation gap at the charge neutrality point at $B_{\mathrm{tot}} = 0$ [Fig. 1(f)] indicative of a substrate-induced sublattice splitting [14]. Consistent with previous results [16,20], the sample shows a series of phase transitions at odd denominator fillings, visible as bulk conductance maxima that mark points at which the bulk energy gap closes or reaches a minimum (Fig. 2). In addition, an even denominator state is observed in the neighborhood of $B_\perp^* \approx 6$ T. Taken together, these data were interpreted [16] as signatures of a transition between charge density wave and antiferromagnetic orders, in which fractional occupation is transferred between the carbon sublattices. However, no sign of the transition is observed in conventional transport at charge neutrality itself, where all the candidate states are electrical insulators, nor do typical electrical measurements give direct insight into the underlying isospin polarization of the fractional states.

To directly probe isospin polarization, we performed electrically actuated magnon transmission measurements [17–19]. The schematic is shown in Fig. 3(a). During the experiment, the Landau level filling factors are fixed at $\nu_{\mathrm{III}} = 2$ and $\nu_{\mathrm{II}} = 1$. The two islands then function as a magnon "injector" and "detector," while region I acts as a magnon "filter," whose density can be tuned by varying V_B. Magnons are generated at the III-II interface in the injector by controlling the chemical potential difference eV_{bias} between copropagating edge states of opposite spin. When the bias exceeds the threshold set by the Zeeman energy, $eV_{\mathrm{bias}}/E_Z > 1$, electrons can scatter between edge states conserving spin and energy by emitting a neutral magnon into the ferromagnetic $\nu_{\mathrm{II}} = 1$ bulk. Here $E_Z = g\mu_B B_{\mathrm{tot}}$ is the Zeeman energy, $g = 2$, and μ_B is the Bohr magneton. When region I also supports long-lived neutral modes that couple strongly to region II magnons, spin and energy can be transmitted across region I to the detector. Within the detector, absorption of a magnon generates a voltage that can be detected via the nonlocal response $\delta V_{\mathrm{nl}}/\delta V_{\mathrm{ex}}$, where δV_{nl} is a finite-frequency nonlocal voltage induced at the detector in response to a small excitation δV_{ex} applied to the injector.

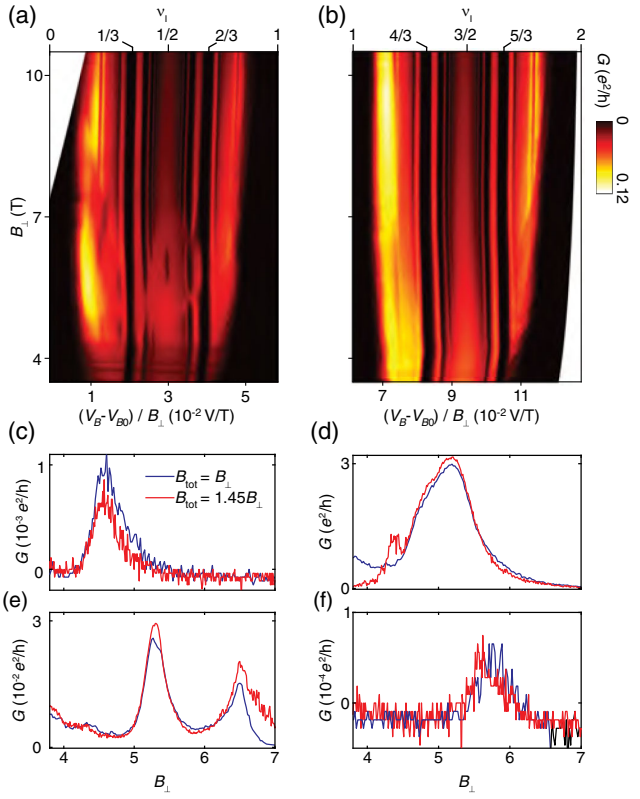

FIG. 2. Signature of isospin phase transition in charge transport measurement. (a) Interisland conductance as function of $B_\perp$ and V_B showing fractional quantum Hall isospin transitions in the range corresponding to Landau level filling factors $0 < \nu_{\mathrm{I}} < 1$. The x axis is offset and scaled by the applied magnetic field so that it is approximately proportional to ν_{I}. (b) Same as (a), measured between $1 < \nu_{\mathrm{I}} < 2$. Isospin phase transitions are absent in this regime. (c) Blue: line cut of (a) at $\nu_{\mathrm{I}} = 1/3$. The maximum in G indicates the isospin phase transition. Red: same as the blue trace, measured with a tilted magnetic field applied. The tilting angle is fixed so that the total magnetic field $B_{\mathrm{tot}} = 1.45B_\perp$. (d) Same as (c), measured at $\nu_{\mathrm{I}} = 2/5$. (e) Same as (c),(d), measured at $\nu_{\mathrm{I}} = 3/5$. (f) Same as (c)–(e), measured at $\nu_{\mathrm{I}} = 2/3$.

Figures 3(b)–3(d) show $\delta V_{\mathrm{nl}}/\delta V_{\mathrm{ex}}$ measured at $\nu_{\mathrm{I}} = 1$, $1/3$, and $2/3$ at magnetic fields both above and below $B_\perp^*$. At $\nu_{\mathrm{I}} = 1$, region I is density matched to the injector and detector, resulting in a large nonlocal response at or slightly above the Zeeman threshold for all B [17,19] corresponding to ferromagnetic magnon transmission through the uniform $\nu_{\mathrm{I}} = 1$ bulk. Similarly, the nonlocal signal is strong both above and below $B_\perp^*$ at $\nu_{\mathrm{I}} = 1/3$, indicating magnon propagation. However, magnon transmission is undetectable at $\nu_{\mathrm{I}} = 2/3$ for $B = 4$ T but is restored at 7 T, indicating a change in the neutral mode spectrum associated with the phase transition observed in local bulk transport measurement. We focus first on the nonlocal signal for $B < B_\perp^*$, shown in Figs. 4(a) and 4(b). Besides $\nu_{\mathrm{I}} = 1$, the strongest nonlocal response is observed at $\nu_{\mathrm{I}} = 5/3$ and over a range

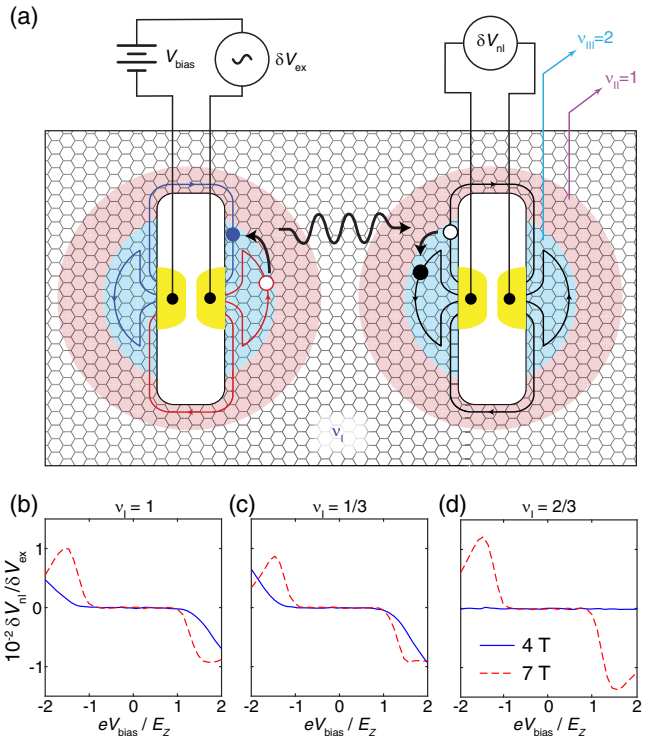

FIG. 3. Electrically detected magnon transmission in the fractional quantum Hall regime. (a) Schematic of magnon transmission experiment on device A. (b) Nonlocal response as function of bias voltage V_{bias} at $\nu_{\mathrm{I}} = 1$, $B_{\perp} = 4$ and 7 T. Curves are acquired at a nominal temperature of 70 mK. (c) Same as (b), measured at $\nu_{\mathrm{I}} = 1/3$. (d) Same as (b), (c), measured at $\nu_{\mathrm{I}} = 2/3$.

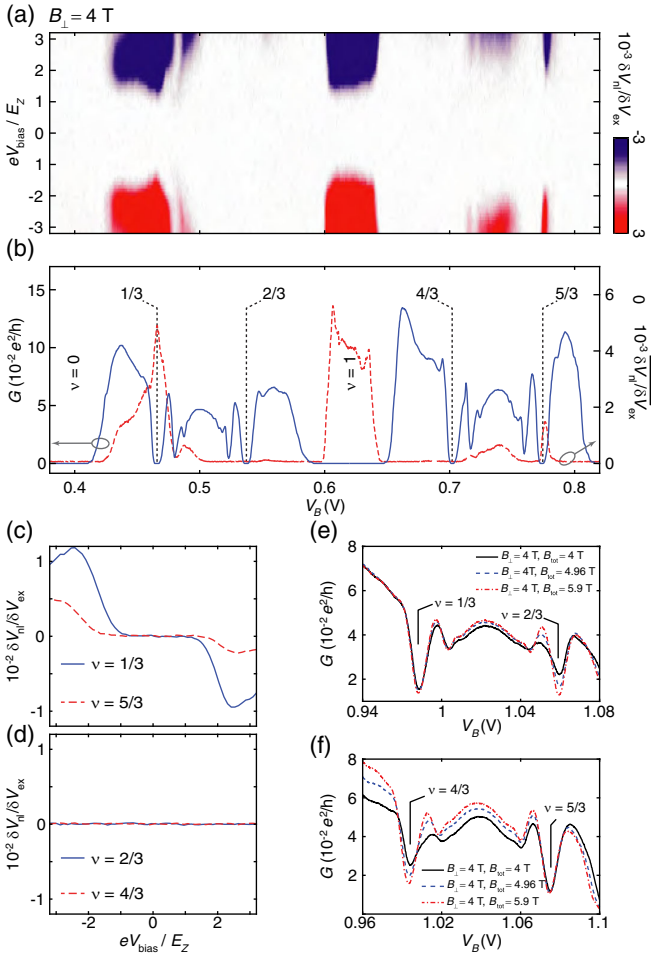

FIG. 4. Contrasting magnon transmission in spin polarized fractional quantum Hall states. (a) Nonlocal response as function of the bottom gate voltage V_B and eV_{bias}/E_Z for $0 < \nu_{\mathrm{I}} < 2$ measured at $B = 4$ T and nominal temperature $T = 50$ mK. (b) Comparison of the root-mean-square average of the data in (b) (red, dashed line) and the local bulk conductance (blue, solid line) as a function of V_B. (c) Nonlocal response at $\nu_{\mathrm{I}} = 1/3, 5/3$ and as a function of eV_{bias}/E_Z, extracted from data in (a). (d) Same as (c), measured at $\nu_{\mathrm{I}} = 2/3, 4/3$. (e) In-plane field dependence of thermally activated conductance of fractional quantum Hall states at $\nu = 1/3$ and $2/3$. The values of perpendicular magnetic field ($B_{\perp}$) and total magnetic field (B_{tot}) are labeled. The measurements were performed at $T = 1.6$ K so that the gaps are thermally excited. (f) Same as (e), measured at $\nu = 4/3$ and $5/3$.

$0.12 < \nu_{\mathrm{I}} < 0.4$ that includes $\nu_{\mathrm{I}} = 1/3$; in contrast, no nonlocal response is observed for even numerator fractional quantum Hall states (2/3 and 4/3).

It is tempting to ascribe the observed even-odd effect to a difference in ground state spin polarization; after all, in the absence of a Zeeman energy the 2/3 and 4/3 states are expected to be spin singlet, and as a consequence should not host propagating spin-wave excitations [21]. However, tilted field magnetotransport measurements [see Figs. 4(e) and 4(f) and Ref. [20]] indicate that the applied $B_{\perp} = 4$ T is sufficient to spin polarize these states. For all spin polarized states, Larmor's theorem dictates that the spin-wave spectrum features at least one mode whose energy increases quadratically as $E(q) \approx E_Z + \hbar^2 q^2/2m$ and whose lifetime diverges as $q \to 0$, with the $q = 0$ Larmor mode corresponding to a uniform rotation of all spins. Consequently, the suppression of magnon transmission for even numerator $n/3$ states cannot arise from an *absence* of spin-wave excitations; rather, it indicates that the specific properties of the spin excitations at fractional filling are incompatible with transmission of ferromagnetic magnons from the $\nu = 1$ quantum Hall ferromagnet. This constitutes a much stronger constraint on the ground state wave function and its excitations than simply sharing a nonzero spin polarization.

For magnon transmission to be observed, region I must host long-lived spin-wave excitations that have significant overlap with the magnons of the $\nu = 1$ quantum Hall ferromagnet over a range of wave vectors, permitting high transmission at the I-II interface, propagation to the second II-I interface, and eventual absorption into the detector. While there is no general theoretical framework to calculate the full spin-wave dispersion for a partially filled Landau level, exact diagonalization of the interacting Hamiltonian is possible at $\nu = 1/3$ and 2/3, and neutral mode spectra

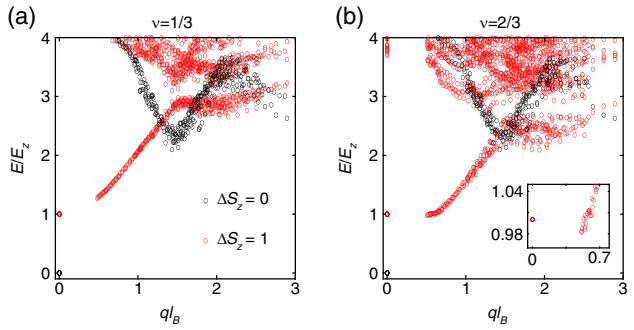

FIG. 5. Spectrum of neutral modes with spin $\Delta S_z = 0$ and 1 measured relative to the ground state for $\nu =$ (a) $1/3$ and (b) $2/3$ at $B_\perp = 4$ T calculated using exact-diagonalization techniques. Here q is the two-dimensional wave vector. $l_B = \sqrt{\hbar/eB}$ is the magnetic length. B is the perpendicular magnetic field.

calculated for monolayer graphene are shown in Fig. 5 (see Appendix B). At $\nu = 1/3$, the spin waves are consistent with a simple evolution of the Larmor mode into a single, monotonically increasing spin-wave branch that eventually merges with a spin-flip continuum for $E/E_Z \approx 3$. In contrast, calculations at $\nu = 2/3$ produce a qualitatively different spin-wave dispersion, in which the mode energy at the lowest finite value of q accessible to the numerical calculations is *lower* than the energy at $q = 0$. This behavior is consistent with a finite momentum "spin-roton minimum" in the dispersion, as previously reported based on both numerical calculations [22,23] and inelastic light scattering measurements [24]. Physically, it arises from the interplay between the strong Zeeman effect, which polarizes the ground state, and Coulomb interactions, which favors an unpolarized state [21]. Finite momentum spin waves correspond to modulations of the ground state spin density that locally lower the spin polarization and thus the Coulomb energy, leading to a spin-roton minimum at finite q (see Appendix C). At $\nu = 2/3$, the spin-flip continuum also appears at lower energy, closer to $E/E_Z \approx 2$.

The calculated spectra suggest several possible explanations for the suppression of magnon transmission at $\nu = 2/3$ (and $4/3$). First, the flatter spin-wave dispersion may decrease the transmission of magnons across the I-II interface due to kinematic constraints, in a magnetic analog of Kapitza resistance. Second, magnons with $E > E_Z$ may decay inelastically into the spin-roton minimum; there, they have energy $E < E_Z$ and consequently cannot enter the detector. Finally, the presence of a lower-lying spin-flip continuum, combined with disorder [25], may provide a damping channel at $\nu = 2/3$ that is not present at $\nu = 1/3$. Indeed, transport measurements suggest that the bottom of the spin-flip continuum lies at $\Delta \sim 1.5E_Z$ for $\nu = 2/3$ and $4/3$ in similar devices [20]. While we are not able to distinguish between these mechanisms in our current experiment—and, indeed, they may all be relevant even at a single filling factor—we note that all are expected to be highly sensitive to the details of the ground state wave

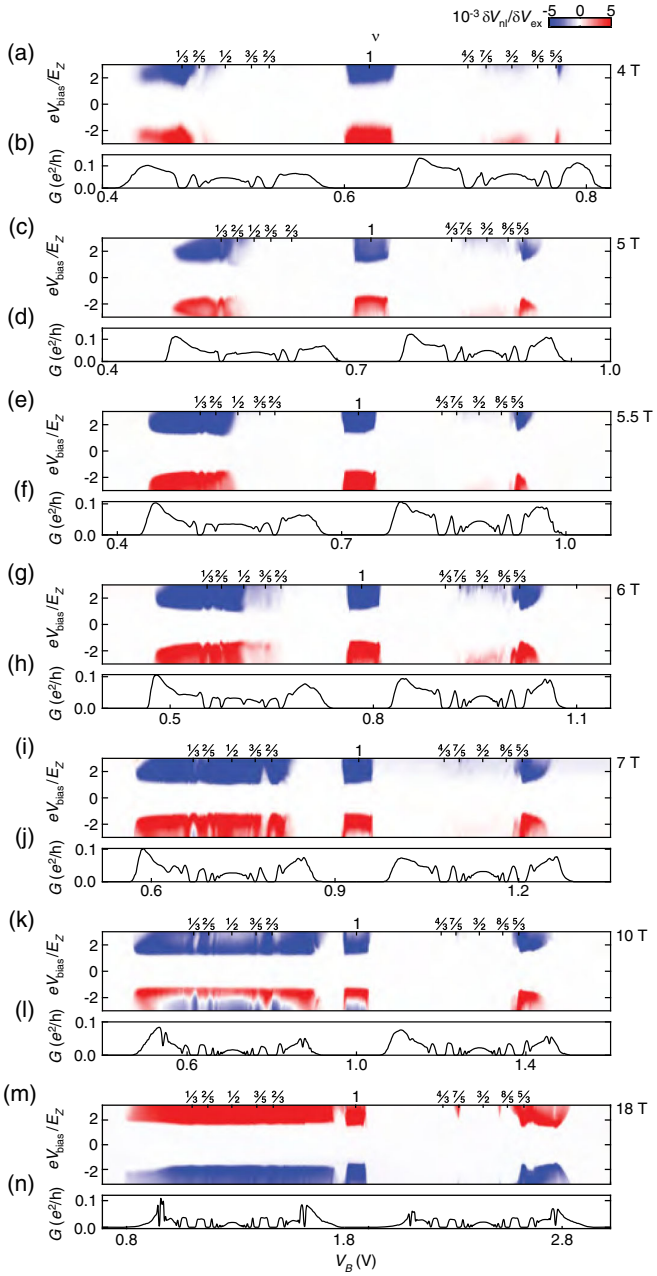

FIG. 6. Magnon transmission at a fractional quantum Hall isospin phase transition. (a) Nonlocal response measured for $0 < \nu_I < 1$ as a function of $eV_{\rm bias}/E_Z$ at $B_\perp = 4$ T. (b) Bulk conductance as a function of V_B measured at $B_\perp = 4$ T. The range of V_B is the same as that in (a). The result is used to calibrate ν_I in (a). (c),(e),(g),(i),(k),(m) Same as (a), measured at $B_\perp = 4$, 5, 5.5, 6, 7, 10, and 18 T, respectively. (d),(f),(h),(j),(l),(n) Same as (b), measured at $B_\perp = 4$, 5, 5.5, 6, 7, 10, and 18 T, respectively.

function and its spin-flip excitations. At the most qualitative level, this is consistent with experiment where an intricate dependence on ν_I is observed both for $0 < \nu_I < 1$ when $B < B^*_\perp$ and for $1 < \nu_I < 2$ at all magnetic fields (Fig. 6). Remarkably, this intricate dependence vanishes at $B > B^*_\perp$, replaced by a density-independent restoration of

magnon transmission across a continuous range of ν_I. As shown in Fig. 6, for $B > B_\perp^*$ the nonlocal signal onsets sharply at the Zeeman threshold—indicating high magnon transmission—throughout the $0 < \nu < 1$ range except for narrow regions near $\nu = 0$ and 1 where signatures of electron solids have been observed [19]. The $B_\perp$-dependent change in transmission cannot be attributed to a change in the ground state spin polarization, as follows from the absence of any dependence of $B_\perp^*$ (or the magnetic fields corresponding to gap closings at odd denominator fillings) on the in-plane magnetic field [see Figs. 2(c)–2(f) and Ref. [16]]. Above $B_\perp^*$ the magnon transmission becomes completely insensitive to the ν-dependent details of the spin-wave dispersion, in apparent conflict with our previous observation that magnon transmission is strongly modulated by the detailed spin-wave spectra of fractional quantum Hall states.

We understand the decoupling of magnon transport from the fractional quantum Hall effect as a consequence of the isospin phase transition thought to underlie the incompressible state at $\nu = \pm 1/2$. Figures 7(a) and 7(b) show the expected isospin polarization above and below $B_\perp^*$, respectively. In both cases, electrons occupy three of the four isospin flavors, leaving the fourth empty.

Below $B_\perp^*$, the underlying order is that of the CDW state, so the low-energy carbon sublattice corresponding to the majority valley K is occupied with both spin projections, $\nu_{K\uparrow} = \nu_{K\downarrow} = 1$. The remaining electrons occupy the available minority sublattice states with the Zeeman favored spin projection, $\nu_{K'\uparrow} = \nu$. Since all available states in the majority valley are completely occupied, the excitation spectrum projected onto the minority valley is identical to a two-component quantum Hall system [26], leading to the situation described in Fig. 4.

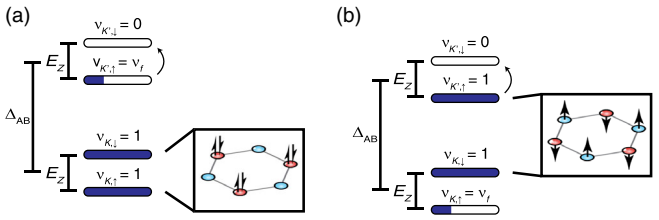

FIG. 7. Schematic of the isospin phase transition. (a) Single particle energy level diagram for the zero Landau level in the low magnetic field regime. The K valley is fully occupied, corresponding to a sublattice polarized state (inset). Additional fractional occupation is in the $K', \uparrow$ level. Spin-1 excitations with $E(q = 0) = E_Z$ consist of excitations between the partially filled and empty K' states, indicated by the arrow. (b) The same diagram but for the high-field phase. Now the underlying order is antiferromagnetic (inset). Spin-1 excitations from the fractionally occupied level are Pauli blocked, with low-energy excitations possible only between the filled $K', \uparrow$ and empty $K', \downarrow$ levels—identical to those of the quantum Hall ferromagnets in the injector and detector.

Above $B_\perp^*$, in contrast, the underlying order is that of the antiferromagnetic (AFM) state, so $\nu_{K'\uparrow} = \nu_{K\downarrow} = 1$ and the remaining electrons occupy the favored sublattice with the Zeeman favored spin projection, $\nu_{K\uparrow} = \nu$. Both spin and sublattice isospins are active. In this case, spin waves in the minority valley involve a transition from a completely occupied Landau level ($\nu_{K'\uparrow} = 1$) to an empty Landau level ($\nu_{K'\downarrow} = 0$). As a result, they are expected to closely resemble excitations within the $\nu = 1$ injector and detector regions. Indeed, within a double-mode approximation that accounts for collective spin-lowering transitions on both sublattices (see Appendix C), we find that the spin-wave stiffness increases only slightly compared to that of the magnons at $\nu = 1$. This is compatible with high transmission of magnons between these ground states and the observed high nonlocal signal.

The onset of nonlocal response across the entire Landau level is thus a direct signature of the transition to antiferromagnetic order. This interpretation is further supported by the contrasting behavior of the nonlocal response for $1 < \nu_I < 2$ (Fig. 6), where antiferromagnetism is not expected and where no such ubiquitous response is observed.

Despite direct evidence for an AFM-CDW transition at $\nu \neq 0$, magnon transmission is not observed near the Zeeman threshold at charge neutrality for any magnetic field. The absence of a signal at low fields is expected, since the CDW phase is nonmagnetic. However, in the high -field phase, a noncollinear canted antiferromagnet is thought to be the ground state because the Zeeman energy favors spin canting when the two sublattices have equal occupation [5,8]. Although prior work [17,18] has reported nonlocal response at $\nu = 0$, it has been observed only at bias voltages far above the Zeeman threshold, where, for example, Joule heating by the injector is non-negligible [19] and high-energy *spinless* collective excitations such as plasmons may also be generated.

Theoretical calculation within the linear spin-wave approximation [27] suggests the absence of a low-energy nonlocal signal is because of the mismatch between the magnon dispersion of $\nu = 0$ CAF and the $\nu = 1$ FM. Additionally, the presence of two magnon modes in the CAF opens up magnon-magnon and other decay channels.

III. CHARGE DENSITY WAVE TO CANTED ANTIFERROMAGNET TRANSITION AT $\nu = 0$

To disentangle these issues and more directly probe the magnon transmission at $\nu = 0$, we introduce a different sample geometry shown in Fig. 8(a). Again, three patterned graphite gates are used to control the charge carrier density in different regions of the monolayer graphene sheet. In this sample, region I is controlled by V_1 and V_2. Region II is controlled by V_1 and V_3, and region III is controlled by V_1. Here, V_1, V_2, and V_3 are the voltages applied to graphite gate 1, 2, and 3, respectively. Figure 8(c) shows the wiring

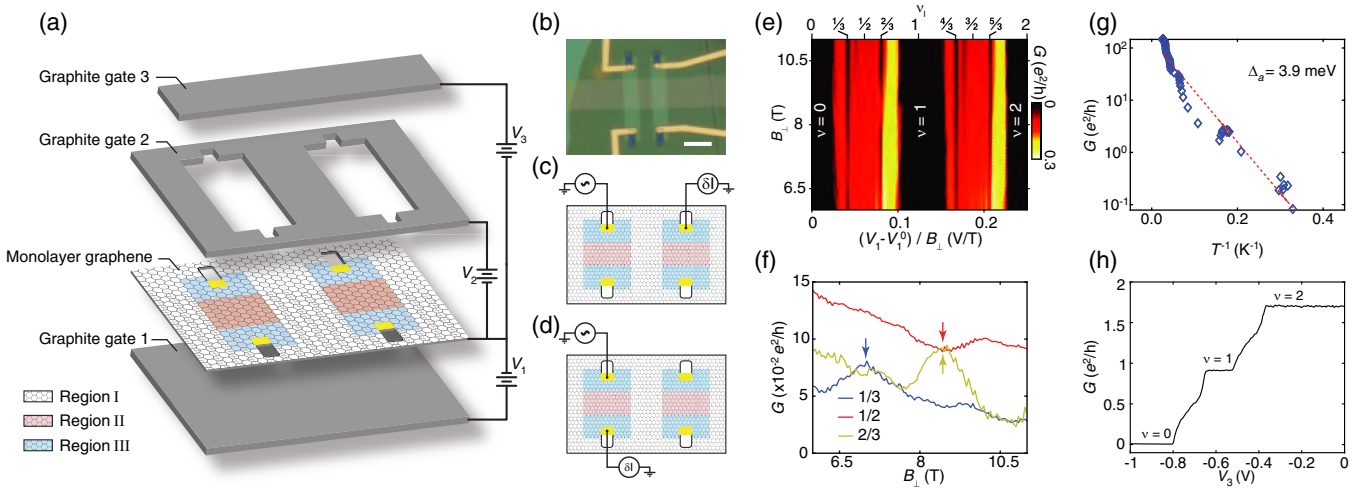

FIG. 8. Charge transport measurement on device A. (a) Device geometry. (b) Optical micrograph of the sample. Scale bar represents 5 μm. (c) Schematic of the interisland transport measurement. (d) Schematic of the intraisland transport measurement. (e) Bulk conductance versus carrier density and magnetic field between $\nu = 0$ to $\nu = 2$, measured in the configuration of (c). (f) Line cuts of (e) along vertical axis at $\nu = 1/3, 1/2$, and $2/3$. Phase transitions at $\nu = 1/3, 2/3$ and the incompressible state at $\nu = 1/2$ are marked by arrows. (g) Arrhenius plot of the conductance at the charge neutrality point; linear fitting of the data shows the sample is insulating with an energy gap of 3.9 meV. (h) A typical trace of intraisland conductance as a function of V_3 measured in the configuration of (d). $V_1 = 0.6131$ V. $V_2 = -0.4717$ V. This combination of V_1 and V_2 ensures $\nu_I = 0$ and $\nu_{III} = 2$.

configuration of the interisland charge transport measurement. Since edge states do not connect the islands, once again interisland transport probes the bulk conductivity as in device A. Figures 8(e) and 8(f) show the result of interisland magnetotransport as a function of V_2 at $0 < \nu_I < 2$. Multiple gap closings are observed at $0 < \nu_I < 1$, and an even denominator fractional quantum Hall state is observed at around $B_\perp = 8$ T, shown as a conductance minimum in Fig. 8(f). Thermal activation gap measurement shows an AB-sublattice splitting of 3.9 meV [Fig. 8(g)]. Device B is thus in the same regime as device A, or devices studied in Ref. [16].

As in the first device geometry, magnon transmission measurements are affected by setting the carrier densities such that $\nu_{II} = 1$ and $\nu_{III} = 2$. This is achieved by using V_1 to control v_{III}, and then tuning V_2 to keep $\nu_I = 0$. Changing ν_{II} can be realized by sweeping V_3. Figure 8(h) shows intraisland transport measured at $B_\perp = 8$ T, showing clear plateaus at these integer filling factors.

Magnon generation and detection follows the same mechanism as in the first device geometry [Fig. 9(a)], with the contact configuration allowing for a potential imbalance between copropagating $\nu = 1$ and $\nu = 2$ edge states. In contrast to device A, however, magnons may be generated directly at a boundary with the $\nu = 0$ state, and nonlocal response need not be mediated by $\nu = 1$ magnons [28]. Figure 9(b) shows the measured nonlocal response in device B. A clear onset of nonlocal response at the Zeeman threshold is observed around $B_\perp = 5$ T, indicating a phase transition from a nonmagnetic phase to a magnetic phase supporting long-range transport of neutral excitations. With an in-plane field applied, the phase transition is shifted to a smaller $B_\perp$ [Fig. 9(c)]. This is in excellent agreement with the expectations for the CAF phase, which is favored by the Zeeman energy as compared to the nonmagnetic CDW phase due to its canted spin structure and finite magnetic moment [5,8].

Our detection of the CDW-AFM transition confirms the theoretically predicted picture of isospin symmetry broken phases in monolayer graphene at charge neutrality. However, we note that our data also raise a number of new questions. While we have focused on the most tractable filling factors of $\nu = 0$ and integer multiples of $1/3$, the magnon data of Figs. 4(a), 4(b), and 6 show a highly featured evolution of the magnon transmission with fractional filling, the precise mechanisms of which remain to be understood. A fuller theoretical interpretation of these features may provide insight into their spin and valley polarizations, as well as the nature of neutral modes in strongly interacting systems more generally. An additional intriguing feature of the data is the qualitative change in the nonlocal signal in sample B in the neighborhood of the $\nu = 1/2$ state [16,20,29,30] shown in Fig. 9(b). Absent a quantitative theory of magnon transmission, this signature is difficult to interpret, but may shed light on the nature of the correlated state, which is currently not well understood. Finally, a mean-field analysis of the phase diagram of the $\nu = 0$ state predicts the existence of a Kekulé distorted PSP phase between the CDW and CAF phases. Future experiments with sensitivity to the sublattice polarization, and theoretical treatments of the magnon transmission in this regime, may shed light on this enigmatic phase.

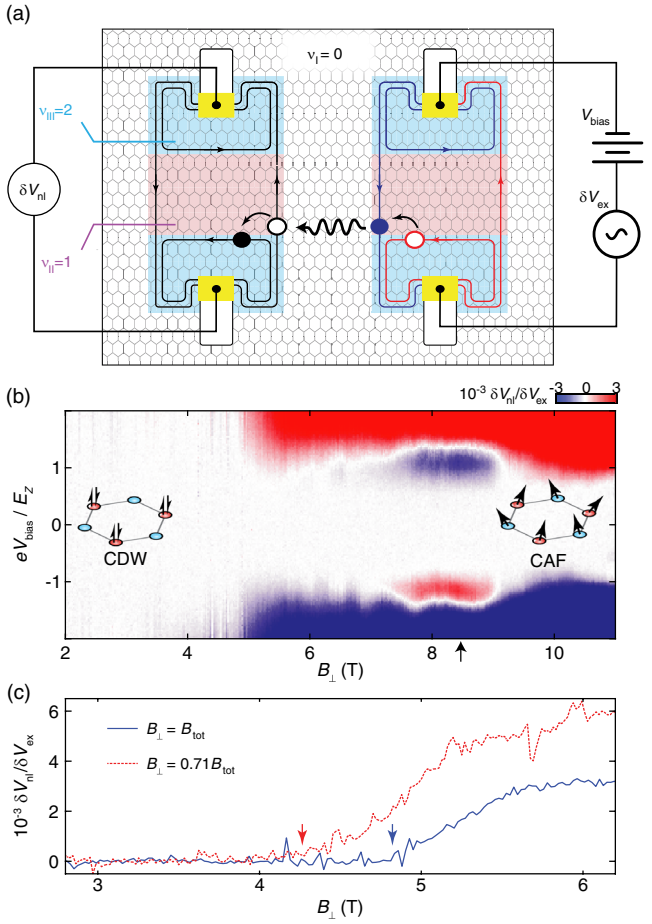

FIG. 9. Charge density wave to canted antiferromagnet transition at $\nu = 0$. (a) Schematic of the experiment. (b) Nonlocal response versus eV_{bias}/E_Z and $B_\perp$ at $\nu_I = 0$. The arrow indicates the value of $B_\perp$ where the incompressible $\nu = 1/2$ state appears. (c) Solid line: line cut of (b) at $eV_{\mathrm{bias}}/E_Z = 1.74$. Dashed line: same measurement with a tilted magnetic field applied. $B_\perp = 0.71B_{\mathrm{tot}}$. The arrows label the value of $B_\perp$ where the nonlocal voltage starts to increase.

ACKNOWLEDGMENTS

A. F. Y. and H. Z. acknowledge discussions with I. Sodemann. A. H. M., C. H., and N. W. acknowledge support from the ARO under Grant No. W911NF-16-1-0472 and from the Welch Foundation under Grant No. F1473. Z. P. acknowledges support by the Leverhulme Trust Research Leadership Grant No. RL-2019-015. M. P. Z. acknowledges support from the ARO through the MURI program (Grant No. W911NF-17-1-0323). Experimental work by H. Z. and A. F. Y. was supported by the National Science Foundation under DMR-1654186. A portion of this work was performed at the National High Magnetic Field Laboratory, which is supported by the National Science Foundation Cooperative Agreement No. DMR-1644779 and the state of Florida. K. W. and T. T. acknowledge support from the Elemental Strategy Initiative conducted by the MEXT, Japan, Grant No. JPMXP0112101001, JSPS KAKENHI Grant No. JP20H00354, and the CREST(JPMJCR15F3), JST.

APPENDIX A: EXPERIMENTAL METHODS

Devices were fabricated using a dry transfer procedure. Sample A was fabricated following Refs. [20,31]. Sample B was fabricated by first assembling and patterning a heterostructure containing monolayer graphene and two graphite gates, and then subsequently transferring the third graphite gate. In both of the devices, hexagonal boron nitride flakes are used to isolate conducting layers, which are not shown in Figs. 1(a) and 8(a).

All data except those in Figs. 6(m) and 6(n) were acquired in a dilution refrigerator equipped with a 14 T superconducting magnet. The measurements were performed at base temperature unless indicated, corresponding to a measured temperature of $T \lesssim 30$ mK on the probe. Data in Figs. 6(m) and 6(n) were performed in a dilution refrigerator equipped with an 18 T superconducting magnet at a base temperature $T \lesssim 50$ mK indicated by the thermometer on the probe. The local bulk conductance and nonlocal voltage measurements on sample A require tuning of the carrier density in regions II and III, following Ref. [19]. The differential conductance was measured using a lock-in amplifier with a 100 μV excitation at 17.777 Hz. The nonlocal voltage was measured using a lock-in amplifier with an ac excitation at 1234.5 Hz with various amplitudes on the order of 100 μV. The frequency is chosen to reduce the noise while maintaining negligible phase shift, and the amplitude is chosen to balance the signal-to-noise ratio and sampling precision. The nonlocal voltage measurements on sample B were performed with an ac excitation of 99.2 μV at 17.777 Hz.

APPENDIX B: METHOD OF EXACT DIAGONALIZATION

Exact diagonalization calculations of the neutral mode spectra were performed using the torus geometry [32]. This geometry, which does not suffer from the ambiguity of "shift" [33], allows us to obtain the exact low-lying energy spectrum at filling factor ν, resolved as a function of a two-dimensional momentum $\mathbf{q}$ [34] and the total z projection of spin S_z of the particles. We diagonalized systems of $N =$ 6–10 electrons (holes) at filling factor $\nu = 1/3$ ($\nu = 2/3$), with up to two spin-flips away from the maximal polarization ($S_z \geq N/2 - 2$). In order to obtain finer resolution of the collective mode, we collated the data corresponding to different types of unit cells, varying the angle between the lattice vectors going from square to hexagonal unit cell, with aspect ratio of the torus fixed to unity. The effective interaction potential is taken from Ref. [35], and includes the dielectric constant $\epsilon_{h-\mathrm{BN}} = \sqrt{\epsilon^{\parallel}\epsilon^{\perp}}$, with $\epsilon^{\perp} = 3.0$ and $\epsilon^{\parallel} = 6.6$, as well as the screening by the graphite gates,

which are accounted for using standard electrostatic calculations, and by the filled Dirac sea at the RPA level [36].

APPENDIX C: MEAN-FIELD THEORY OF MAGNON TRANSMISSION

In this Appendix, we discuss magnon transmission for a device geometry consisting of an integer quantum Hall ferromagnet with filling faction $\nu_{\rm II} = 1$ and a state at filling fraction $0 < \nu_{\rm I} < 1$. Reference [27] presents microscopic calculations of the magnon transmission probability for the case of $\nu_{\rm I} = 0$ and $\nu_{\rm I} = -1$ using time-dependent Hartree-Fock theory. The result is that the average magnon transmission for $\nu_{\rm I} = 0$ canted antiferromagnet is lower than $\nu_{\rm I} = -1$ ferromagnet. This is because the magnon dispersion of the CAF is stiffer than FM, so the energy and transverse-momentum conservation limits the available phase space for transmission. This effect resembles that underlying Kapitza heat resistance [37]. Based on the idea of energy mismatch, we proceed to give a rough estimate of magnon transmission probability. We assume the long-wavelength magnon dispersion in the $\nu_{\rm I}$ region is parametrized by a density-dependent spin stiffness ρ_ν: $\hbar\omega_\nu(q) = E_Z + \rho_\nu q^2$. Because of the quadratic dispersion, a magnon's equation of motion satisfies the Schrödinger equation and we solve it via elementary means:

$$\begin{aligned}\psi(x) &= Ae^{iq_L x} + Be^{-iq_L x}, \qquad x < 0,\\ &= Ce^{iq_R x}, \qquad x > 0,\end{aligned} \tag{C1}$$

where $\rho_1 q_L^2 = \rho_{\nu_1} q_R^2$. Current conservation and wave function continuation imposes the following boundary conditions:

$$\rho_1 q_L (A - B) = \rho_{\nu_1} q_R, \qquad A + B = C. \tag{C2}$$

By solving the above equations, we obtain the ratio of the transmitted and injected spin current as follows:

$$T = \frac{j_{\rm trans}}{j_{\rm tot}} = \frac{\rho_{\nu_1} q_R |C|^2}{\rho_1 q_L |A|^2} = \frac{4\sqrt{\rho_1 \rho_{\nu_1}}}{(\sqrt{\rho_1} + \sqrt{\rho_{\nu_1}})^2}. \tag{C3}$$

We shall now estimate the magnon dispersion for the weak-field CDW-like state and the strong-field AFM-like state.

1. Magnon transmission below the critical field

For the weak-field state $|\Psi_L\rangle$, the majority valley is fully occupied with both spin projections while the minority fractionally occupied the Zeeman favored spin projection [Fig. 7(a)]. As a result, the ground state has the following property:

$$s_i^+ |\Psi_L\rangle = \tau_i^+ |\Psi_L\rangle = 0, \quad \forall\ i = 1, 2, \ldots, N_e, \tag{C4}$$

where N_e is the number of electrons where s_i^+ and τ_i^+ are, respectively, the spin and valley creation operators.

The zero energy Landau level projected spin lowering operator is given by the following operator:

$$S^-_{q,B} = \sum_j e^{i\vec{q}\cdot\vec{R}_j} \frac{1 - \tau_j^z}{2} s_j^-. \tag{C5}$$

This operator acts on the guiding center coordinate $\vec{R}$ of all the electrons and creates a single magnon in minority valley (K') with wave vector $\vec{q}$.

The single-mode approximation (SMA) assumes the spectral weight of spin-1 excitations at wave vector $\vec{q}$ is mainly concentrated at the energy $\hbar\omega_v(\vec{q})$, which is the energy required to create $S^-_{q,B}|\psi_L\rangle$. This approximation is exact at $q = 0$ since it satisfies Larmor's theorem and it remains a good approximation in the long-wavelength limit.

Starting from the Heisenberg equation of motion, we arrive at the familiar equation for the SMA:

$$\omega_\nu(\vec{q}) = \frac{\langle [S^+_{-q,B}, [H, S^-_{q,B}]]\rangle}{\langle S^+_{-q,B} S^-_{q,B}\rangle}, \tag{C6}$$

where $\langle\rangle$ denotes the expectation value with respect to $|\Psi_L\rangle$. The Hamiltonian projected to the zero Landau level is given by the following:

$$H = H_0 + H_z + H_\perp - \frac{\Delta_{AB}}{2}\tau^z_{k=0} - \frac{\Delta_z}{2} S^z_{k=0}, \tag{C7}$$

$$H_0 = \frac{1}{2A}\sum_k g_0(k)\rho_{-k}\rho_k, \tag{C8}$$

$$H_z = \frac{1}{2A}\sum_k g_z(k)\tau^z_{-k}\tau^z_k, \tag{C9}$$

$$H_\perp = \frac{1}{4A}\sum_k g_\perp(k)(\tau^+_{-k}\tau^-_k + \tau^-_{-k}\tau^+_k). \tag{C10}$$

Here we defined $\rho_k = \sum_j e^{i\vec{k}\cdot\vec{R}_j}$ and $\Gamma_k = \sum_j e^{i\vec{k}\cdot\vec{R}_j}\Gamma_j$ for arbitrary combination Γ of Pauli matrices.

$$g_0(k) = \frac{e^2}{\epsilon}\frac{2\pi}{k} e^{-k^2 l_B^2/2}, \qquad g_{z/\perp}(k) = g_{z/\perp} e^{-k^2 l_B^2/2}. \tag{C11}$$

Using the commutation relation $[R_i^\mu, R_j^\nu] = -il_B^2 \epsilon^{\mu\nu}\delta_{ij}$, $(\mu, \nu = \{x, y\})$, we can evaluate the following double commutators for later convenience:

$$[S^+_{-q,\alpha},[H_0+H_z,S^-_{q,\alpha}]]=\frac{4}{A}\sum_k[g_0(k)+g_z(k)]\sin^2\left(\frac{k\wedge q}{2}\right)\left(\frac{1}{2}\{S^+_{-k-q,\alpha},S^-_{k+q,\alpha}\}-\rho_{-k}\rho_k\right), \tag{C12}$$

$$[S^+_{-q,\beta},[H_\perp,S^-_{q,\alpha}]]=\frac{c_\alpha c_\beta}{2}\sum_k g_\perp(k)e^{(i/2)\vec{k}\wedge\vec{q}(c_\alpha-c_\beta)}\Big[\{(\tau^+s^+)_{-k-q},(\tau^-s^-)_{k+q}\}$$
$$+\{(\tau^-s^+)_{k-q},(\tau^+s^-)_{k+q}\}-4\left\{\left(\tau^-\frac{1-s^z}{2}\right)_k,\tau^+_{-k}\right\}-4\left\{\left(\tau^+\frac{1+s^z}{2}\right)_{-k},\tau^-_k\right\}\Big], \tag{C13}$$

where $\alpha,\beta=\{A,B\}$ and $c_\alpha=1(-1)$ for $\alpha=A(B)$. In this section, we are only interested in $\alpha=\beta=B$. Substituting the above two equations into Eq. (C6), applying Eq. (C4) to simplify the expression and using the spin susceptibilty,

$$\langle S^+_{-q,B}S^-_{q,B}\rangle=4N_{B\uparrow}, \tag{C14}$$

where $N_{s,\alpha}$ is the electron number on sublattice α with spin s, we derive the magnon dispersion and spin stiffness:

$$\omega_\nu(\vec{q})=E_z+\frac{2}{A}\sum_k[g_o(k)+g_z(k)]\sin^2\left(\frac{k\wedge q}{2}\right)[1-\mathcal{S}_\nu(k)], \tag{C15}$$

$$\rho_\nu=\frac{1}{4}\int\frac{d^2k}{(2\pi)^2}[g_o(k)+g_z(k)]k^2[1-\mathcal{S}_\nu(k)]. \tag{C16}$$

Here, $\mathcal{S}_\nu(k)=N^{-1}_{B\uparrow}\langle\rho_{-k}\rho_k\rangle$ is the static structure factor. It has the following properties: (1) $\mathcal{S}_\nu(k)$ is only nonvanishing in the fractionally occupied Landau level, i.e., $\mathcal{S}_1(k)=0$, and (2) $\mathcal{S}_\nu(k)$ satisfies the following equation under particle-hole transformation, $\nu\mathcal{S}_\nu(k)=(1-\nu)\mathcal{S}_{1-\nu}(k)$ for $k\neq 0$. Using these properties and Eq. (C15), we arrive at the following equation relating the mode frequencies at different ν:

$$\omega_\nu=\left(2-\frac{1}{\nu}\right)\omega_1+\left(\frac{1}{\nu}-1\right)\omega_{1-\nu}. \tag{C17}$$

For $\nu=1$, the spin stiffness can be easily calculated from Eq. (C16), which yields $\rho_1=\sqrt{2\pi}e^2/8\epsilon l_B+u_z/2$. For $\nu=1/3$, we use the static structure factor evaluated in Ref. [38] to calculate the spin stiffness $\rho_{1/3}$. When the ground state of $\nu=2/3$ is assumed to be the particle-hole conjugation of the fully spin polarized $\nu=1/3$ Laughlin state, we can use Eq. (C17) to estimate the magnon excitation energy. This leads to the following result:

$$\rho_{1/3}\approx 0.035\frac{e^2}{\epsilon l_B}\overset{B=4T}{=}0.1\rho_1, \tag{C18}$$

$$\rho_{2/3}=\frac{1}{2}(\rho_1+\rho_{1/3})\overset{B=4T}{=}0.55\rho_1. \tag{C19}$$

The SMA predicts that the magnon excitation energy at finite q is always larger than the Larmor mode at $q=0$. When we substitute their dispersions into Eq. (C3) to estimate the transmission probability, we arrive at

$$T_{1/3}=73\%,\qquad T_{2/3}=98\%. \tag{C20}$$

For $\nu=1/3$, the SMA is in good agreement with finite-size exact-diagonalization calculation [39] for small q. For $\nu=2/3$, the SMA fails to produce the spin-roton minimum revealed by exact diagonalization (as shown in Fig. 5(b) of main text and described in the associated discussion). Evidently, substantial spin-flip spectral weight is placed in higher-energy states that are not captured in the SMA, leading to a discrepancy with the experiment.

2. Spin roton at integer filling fractions

In order to gain simple physical understanding of the spin-roton minimum at $\nu=2/3$, we consider a simplified model system of a two-component system at filling 2—i.e., an integer filling factor analog of the $\nu=2/3$ state. The Hamiltonian is given by the following:

$$H=\sum_{n,m,\sigma}(n\hbar\omega+\sigma E_z/2)c^\dagger_{nm\sigma}c_{nm\sigma}+\frac{1}{2}\sum_{\vec{q}}\sum_{n_{1,2,3,4}}\bar{V}_{n_4,n_3,n_2,n_1}(\vec{q})[\bar{\rho}_{n_4n_1}(-\vec{q})\bar{\rho}_{n_3n_2}(\vec{q})-\delta_{n_3,n_1}\bar{\rho}_{n_4n_2}(0)], \tag{C21}$$

$$\bar{V}_{n_4,n_3,n_2,n_1}(\vec{q}) = V(\vec{q})F_{n_4n_1}(-\vec{q})F_{n_3n_2}(\vec{q}), \tag{C22}$$

where $c_{nm\uparrow/\downarrow}$ annihilates a spin-up or spin-down electron in the mth guiding center and the nth Landau level. The form factor $F_{n'n}$ and the projected density operator $\bar{\rho}_{n'n}$ read

$$F_{n'n}(\vec{q}) = \langle n'|e^{-i\vec{q}\cdot(-\vec{\Pi}\times\hat{z})l_B^2}|n\rangle = \sqrt{\frac{2^{l'}l'!}{2^l l!}}[-iq_x + q_y\mathrm{sgn}(n'-n)]^{l-l'}L_{l'}^{l-l'}\left(\frac{\vec{q}^2}{2}\right)e^{-q^2/4}, \tag{C23}$$

$$\rho_{n'n}(\vec{q}) = \sum_{m',m,\sigma}\langle m'|e^{-i\vec{q}\cdot\vec{R}}|m\rangle c^\dagger_{n'm'\sigma}c_{nm\sigma}, \tag{C24}$$

where $l \equiv \max\{n,n'\}, l' \equiv \min\{n,n'\}$, and $L_l^{l'}(x)$ is the generalized Laguerre polynomial. We express the interaction Hamiltonian in terms of the projected density operator at the cost of an additional term proportional to $\bar{\rho}_{n'n}(0)$ to correct the ordering of fermion operators. This additional term cannot be dropped if the Hilbert space includes more than one Landau level since it in general does not commute with the first part of the interaction Hamiltonian. Let us calculate the dispersion of spin-flip collective modes within the Hilbert space spanned by $n = 0$, 1 Landau levels at $\nu = 2$. When the exchange energy is the most dominant energy scale, the ground state is a quantum Hall ferromagnet (QHF): a Slater determinant with electrons occupying the spin-up states of the $n = 0$ and $n = 1$ Landau levels. Using the equation of motion described in the last section, we arrive at the following eigenvalue equation:

$$\sum_{n_2,n_1=0}^{1}[\omega\chi_{n_4n_3,n_2n_1} - \Omega_{n_4n_3,n_2n_1}(\vec{q})]Y_{n_2n_1}(\vec{q}) = 0, \tag{C25}$$

where

$$\chi_{n_4n_3,n_2n_1} = \delta_{n_4,n_2}\delta_{n_3,n_1}\langle S^+_{n_4n_3}(\vec{q})S^-_{n_2n_1}(\vec{q})\rangle = \delta_{n_4,n_2}\delta_{n_3,n_1}N_\phi, \tag{C26}$$

$$\Omega_{n_4n_3,n_2n_1} = \langle[\bar{S}^+_{n_4n_3}(-\vec{q}),[H,\bar{S}^-_{n_2n_1}(\vec{q})]]\rangle \tag{C27}$$

$$= [(n_2-n_1)\hbar\omega + E_z]\chi_{n_4n_3,n_2n_1} + \sum_{\vec{q},n'}\bar{V}_{n_1n'n_4n'}(\vec{q}')\delta_{n_2n_3}N_\phi - \sum_{\vec{q}}\bar{V}_{n_1n_3n_2n_4}(\vec{q}')\cos(\vec{q}'\wedge\vec{q})N_\phi, \tag{C28}$$

$$\bar{S}^-_{n',n}(\vec{q}) = \sum_{m',m}|m'\rangle e^{-i\vec{q}\cdot\vec{R}}|m\rangle c^\dagger_{n'm'\downarrow}c_{nm\uparrow}, \tag{C29}$$

and N_ϕ is the number of flux quanta. To derive this equation, we have used the following properties of the quantum Hall ferromagnet:

$$\bar{S}^+_{n'n}(\vec{q})|\Psi_{\mathrm{QHF}}\rangle = 0, \tag{C30}$$

$$\bar{\rho}_{n'n}(\vec{q})|\Psi_{\mathrm{QHF}}\rangle = \delta_{\vec{q},0}\delta_{n'n}N_\phi. \tag{C31}$$

At a given q, Eq. (C25) is a 4×4 matrix equation whose eigenvalues correspond to the four spin-flip collective modes plotted in Figs. 10(a) and 10(b), where energy is measured relative to the Zeeman energy. Note there is always a mode with energy exactly equal to E_z at $\vec{q} = 0$, as required by Larmor's theorem. Increasing the cyclotron energy will lower the energies of spin-flip transitions that lower the LL index. This mode will mix with the Larmor mode at finite momentum $q = q^*$ and the consequent level-repulsion effect leads to a "spin-roton" minimum when $\hbar\omega_c$ is sufficiently large.

In this calculation, the ground state is always assumed to be a QHF with maximum spin polarization because the energy that favors a spin polarized phase (exchange energy plus Zeeman energy) is bigger than the energy that favors a spin unpolarized phase (cyclotron energy), i.e., $(\Delta_{\mathrm{ex}} + E_Z)/\hbar\omega_c > 1$. Note typically $\Delta_{\mathrm{ex}} \gg E_Z$. As the ratio approaches one from above, $(\Delta_{\mathrm{ex}} + E_Z)/\hbar\omega_c \to 1^+$, the spin-flip excitation spectrum of the QHF develops a deeper spin-roton minimum, as shown in Figs. 10(a) and 10(b). This is because the energy of the spin unpolarized state favored by $\hbar\omega_c$ becomes nearly degenerate to the ground state energy of the QHF.

At $\nu = 2/3$, the Coulomb energy favors a spin-singlet state. When the Zeeman energy wins over the Coulomb energy, the ground state is spin polarized and its spin-flip excitation also shows a shallow spin-roton minimum. The integer calculation suggests that this spin-roton minimum could arise from the competition between the spin polarized state and the spin-singlet state. However, since the Zeeman energy merely provides a q-independent shift to the spin-flip spectrum, the characteristics of the spin-roton minimum (e.g., position and depth) are determined solely by the Coulomb energy.

Despite the difference between $\nu = 2$ and $\nu = 2/3$ excited wave functions, their spin-roton dispersion is similar and this is sufficient to suppress magnon transmission into the stiffer $\nu = 1$. By conservation of energy and transverse momentum q_y, we equate

$$\omega_{\mathrm{rot}}(q_{x,\mathrm{in}}, q_y) = \omega_{\nu=1}(q_{x,\mathrm{out}}, q_y), \tag{C32}$$

where $\omega_{\nu=1}$ is the magnon dispersion of $\nu = 1$ and ω_{rot} is plotted in Fig. 10(c). Because ω_1 is stiffer than ω_{rot}, $q_{x,\mathrm{out}}$ becomes imaginary when the incident angle $\tan^{-1}(q_y/q_{x,\mathrm{in}})$ is large. The average transmission rate at low energy is thus reduced to less than 40%, already a large suppression compared to the 98% transmission obtained by the naive SMA approximation [Fig. 10(d)].

3. Magnon transmission above the critical field

For $B > B_{\perp}^{*}$, the high-field configuration $|\Psi_H\rangle$ is shown in Fig. 7(b). We study magnon dispersion using the natural generalization of single-mode approximation. In metallic ferromagnets, magnons can be emitted when minority spin electron change to majority spin electron $e\downarrow \to e\uparrow$ and when majority spin hole change to minority spin hole $h\uparrow \to h\downarrow$. Similarly, magnons in $|\Psi_H\rangle$ can be created by $e\downarrow \to e\uparrow$ in the minority valley ($K' = B$) and $h\uparrow \to h\downarrow$ in the majority valley ($K = A$). Hence, the spin-lowering process is in general a linear combination of the two valleys:

$$O_q^{\dagger} = Y_q S_{qA}^{-} + Z_q S_{qB}^{-}. \tag{C33}$$

Using the equation of motion method, we arrive at the following:

$$\hbar\omega_q \begin{pmatrix} \chi_{AA} & 0 \\ 0 & \chi_{BB} \end{pmatrix} \cdot \begin{pmatrix} Y_q \\ Z_q \end{pmatrix} = \begin{pmatrix} \Omega_{AA} & \Omega_{AB} \\ \Omega_{BA} & \Omega_{BB} \end{pmatrix} \begin{pmatrix} Y_q \\ Z_q \end{pmatrix}, \tag{C34}$$

where

$$\chi_{ij} = \langle S_{-qi}^{+} S_{qj}^{-} \rangle, \quad \Omega_{ij} = \langle [S_{-qi}^{+}, [H, S_{qj}^{-}]] \rangle, \quad i,j = \{A,B\}, \tag{C35}$$

and $\langle\rangle$ denotes the expectation value of the high-field ground state $|\Psi_H\rangle$. The static susceptibility can be easily evaluated to give

$$\chi_{ii} = 4(N_{i\uparrow} - N_{i\downarrow}). \tag{C36}$$

The frequency matrix is slightly more complicated. Using Eqs. (C12) and (C13), we found

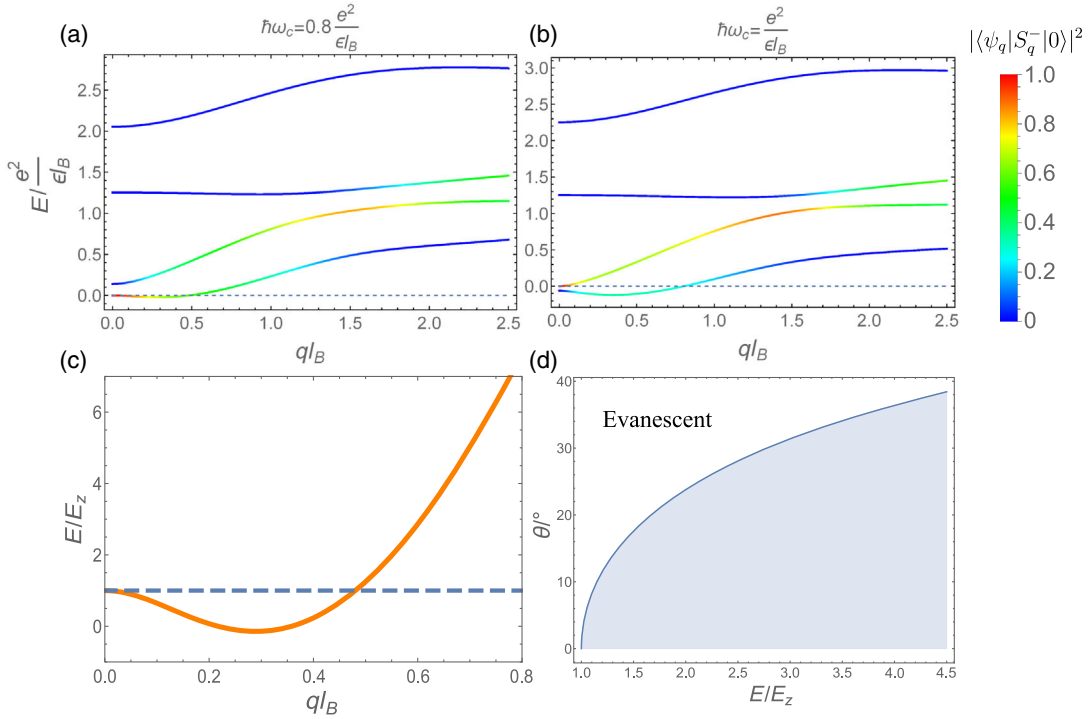

FIG. 10. The energy E of the four spin-flip collective modes in the $N = 0$, 1 LL with the cyclotron energy (a) $\hbar\omega_c = 0.8e^2/\epsilon l_B$ and (b) $e^2/\epsilon l_B$. The Zeeman energy is not included since it only produces a constant shift of all these dispersions. The line color stands for the overlap between the normal modes $|\psi_q\rangle$ and the single magnon wave function ansatz $S_q^-|0\rangle$, which is exactly one for the $q = 0$ Larmor mode. (c) The low-energy dispersion of the lowest mode in (a). Here we include the Zeeman energy. (d) The phase space of magnon transmission in the incident angle-energy plane. When the incident angle from $\nu = 2$ QHF onto the $\nu = 1$ QHF becomes large, they become evanescent in the $\nu = 1$ region.

$$\frac{\Omega_{AA}(q)}{\chi_{AA}} = \Delta_z + \frac{2}{A}\sum_k [g_o(k) + g_z(k)]\sin^2\left(\frac{k \wedge q}{2}\right)[-1 + \mathcal{S}_\nu(k)] + \frac{u_\perp D}{2\chi_{AA}}$$
$$= \Delta_z - \rho_{1/3} q^2 + O(q^4), \tag{C37}$$

$$\frac{\Omega_{BB}(q)}{\chi_{BB}} = \Delta_z + \frac{2}{A}\sum_k [g_o(k) + g_z(k)]\sin^2\left(\frac{k \wedge q}{2}\right) + \frac{u_\perp D}{2\chi_{BB}}$$
$$= \Delta_z + u_\perp \frac{D}{2\chi_{BB}} + \rho_1 q^2 + O(q^4), \tag{C38}$$

$$\frac{\Omega_{AB}(q)}{\chi_{AA}} = -\frac{u_\perp D}{2\chi_{AA}} e^{-q^2 l_B^2/2}, \tag{C39}$$

$$\frac{\Omega_{BA}(q)}{\chi_{BB}} = -\frac{u_\perp D}{2\chi_{BB}} e^{-q^2 l^2/2}, \tag{C40}$$

where we define

$$D = 8[N_{A\uparrow} + (N_{A\uparrow} - N_{B\uparrow}) - (N_{A\downarrow} - N_{B\downarrow})], \tag{C41}$$

$$\mathcal{S}_\nu(k) = \frac{\langle \rho_{kA}\rho_{-kA}\rangle}{|N_{A\uparrow} - N_{A\downarrow}|} \equiv \frac{\langle (1+\tau^z)_{-k}(1+\tau^z)_k\rangle}{4|N_{A\uparrow} - N_{A\downarrow}|}, \tag{C42}$$

and also used the following properties of the $|\Psi_H\rangle$:

$$S^-_{q,A}|\Psi_H\rangle = S^+_{q,B}|\Psi_H\rangle = (\tau^+ s^-)_q|\Psi_H\rangle = (\tau^- s^+)_q|\Psi_H\rangle = 0. \tag{C43}$$

The normal mode frequency, $\omega_q = \Delta_z + \rho^{(H)}_{2/3} q^2 + O(q^4)$,

$$\rho^{(H)}_{2/3} = \frac{\rho_1 - \rho_{1/3}}{2} + \frac{\rho_1 + \rho_{1/3}}{2}\frac{\chi_{BB} - \chi_{AA}}{\chi_{BB} + \chi_{AA}} - \frac{u_\perp D}{2(\chi_{BB} + \chi_{AA})}$$
$$\overset{B=8T}{=} 1.9\rho_1. \tag{C44}$$

We see that the antiferromagnetic coupling between the spin in the two sublattices makes the magnon stiffer. The transmission probability, $T \approx 98\%$, of $\nu = 1|2/3$ interface at high field is higher than the low field.

[1] H. A. Fertig and L. Brey, *Luttinger Liquid at the Edge of Undoped Graphene in a Strong Magnetic Field*, Phys. Rev. Lett. **97**, 116805 (2006).

[2] D. A. Abanin, P. A. Lee, and L. S. Levitov, *Spin-Filtered Edge States and Quantum Hall Effect in Graphene*, Phys. Rev. Lett. **96**, 176803 (2006).

[3] I. F. Herbut, *Theory of Integer Quantum Hall Effect in Graphene*, Phys. Rev. B **75**, 165411 (2007).

[4] J. Jung and A. H. MacDonald, *Theory of the Magnetic-Field-Induced Insulator in Neutral Graphene Sheets*, Phys. Rev. B **80**, 235417 (2009).

[5] M. Kharitonov, *Phase Diagram for the $\nu = 0$ Quantum Hall State in Monolayer Graphene*, Phys. Rev. B **85**, 155439 (2012).

[6] K. Nomura, S. Ryu, and D.-H. Lee, *Field-Induced Kosterlitz-Thouless Transition in the $n = 0$ Landau Level of Graphene*, Phys. Rev. Lett. **103**, 216801 (2009).

[7] M. Kharitonov, *Canted Antiferromagnetic Phase of the $\nu = 0$ Quantum Hall State in Bilayer Graphene*, Phys. Rev. Lett. **109**, 046803 (2012).

[8] D. A. Abanin, B. E. Feldman, A. Yacoby, and B. I. Halperin, *Fractional and Integer Quantum Hall Effects in the Zeroth Landau Level in Graphene*, Phys. Rev. B **88**, 115407 (2013).

[9] I. Sodemann and A. H. MacDonald, *Broken SU(4) Symmetry and the Fractional Quantum Hall Effect in Graphene*, Phys. Rev. Lett. **112**, 126804 (2014).

[10] A. F. Young, J. D. Sanchez-Yamagishi, B. Hunt, S. H. Choi, K. Watanabe, T. Taniguchi, R. C. Ashoori, and P. Jarillo-Herrero, *Tunable Symmetry Breaking and Helical Edge Transport in a Graphene Quantum Spin Hall State*, Nature (London) **505**, 528 (2014).

[11] L. Veyrat *et al.*, *Helical Quantum Hall Phase in Graphene on* $SrTiO_3$, Science **367**, 781 (2020).

[12] J. Lee and S. Sachdev, *Deconfined Criticality in Bilayer Graphene*, Phys. Rev. B **90**, 195427 (2014).

[13] J. Lee and S. Sachdev, *Wess-Zumino-Witten Terms in Graphene Landau Levels*, Phys. Rev. Lett. **114**, 226801 (2015).

[14] B. Hunt *et al.*, *Massive Dirac Fermions and Hofstadter Butterfly in a van der Waals Heterostructure*, Science **340**, 1427 (2013).

[15] F. Amet, J. R. Williams, K. Watanabe, T. Taniguchi, and D. Goldhaber-Gordon, *Insulating Behavior at the Neutrality Point in Single-Layer Graphene*, Phys. Rev. Lett. **110**, 216601 (2013).

[16] A. A. Zibrov, E. M. Spanton, H. Zhou, C. Kometter, T. Taniguchi, K. Watanabe, and A. F. Young, *Even-Denominator Fractional Quantum Hall States at an Isospin Transition in Monolayer Graphene*, Nat. Phys. **14**, 930 (2018).

[17] D. S. Wei, T. van der Sar, S. H. Lee, K. Watanabe, T. Taniguchi, B. I. Halperin, and A. Yacoby, *Electrical Generation and Detection of Spin Waves in a Quantum Hall Ferromagnet*, Science **362**, 229 (2018).

[18] P. Stepanov *et al.*, *Long-Distance Spin Transport through a Graphene Quantum Hall Antiferromagnet*, Nat. Phys. **14**, 907 (2018).

[19] H. Zhou, H. Polshyn, T. Taniguchi, K. Watanabe, and A. F. Young, *Solids of Quantum Hall Skyrmions in Graphene*, Nat. Phys. **16**, 154 (2020).

[20] H. Polshyn, H. Zhou, E. M. Spanton, T. Taniguchi, K. Watanabe, and A. F. Young, *Quantitative Transport Measurements of Fractional Quantum Hall Energy Gaps in Edgeless Graphene Devices*, Phys. Rev. Lett. **121**, 226801 (2018).

[21] B. I. Halperin, *Theory of the Quantized Hall Conductance*, Helv. Phys. Acta **56**, 75 (1983), https://www.e-periodica.ch/digbib/view?pid=hpa-001:1983:56::1243#87.

[22] S. S. Mandal and J. K. Jain, *Low-Energy Spin Rotons in the Fractional Quantum Hall Effect.*, Phys. Rev. B **63**, 201310 (R) (2001).

[23] D. Majumder and S. S. Mandal, *Neutral Collective Modes in Spin-Polarized Fractional Quantum Hall States at Filling Factors* $1/3$*,* $2/5$*,* $3/7$*, and* $4/9$, Phys. Rev. B **90**, 155310 (2014).

[24] U. Wurstbauer *et al.*, *Observation of Nonconventional Spin Waves in Composite-Fermion Ferromagnets*, Phys. Rev. Lett. **107**, 066804 (2011).

[25] C. Kallin and B. I. Halperin, *Many-Body Effects on the Cyclotron Resonance in a Two-Dimensional Electron Gas*, Phys. Rev. B **31**, 3635 (1985).

[26] K. Moon, H. Mori, K. Yang, S. M. Girvin, A. H. MacDonald, L. Zheng, D. Yoshioka, and S-C. Zhang, *Spontaneous Interlayer Coherence in Double-Layer Quantum Hall Systems: Charged Vortices and Kosterlitz-Thouless Phase Transitions*, Phys. Rev. B **51**, 5138 (1995).

[27] N. Wei, C. Huang, and A. H. MacDonald, *Scattering of Magnons at Graphene Quantum-Hall-Magnet Junctions*, Phys. Rev. Lett. **126**, 117203 (2021).

[28] S. Takei, A. Yacoby, B. I. Halperin, and Y. Tserkovnyak, *Spin Superfluidity in the* $\nu = 0$ *Quantum Hall State of Graphene*, Phys. Rev. Lett. **116**, 216801 (2016).

[29] S. Narayanan, B. Roy, and M. P. Kennett, *Incompressible Even Denominator Fractional Quantum Hall States in the Zeroth Landau Level of Monolayer Graphene*, Phys. Rev. B **98**, 235411 (2018).

[30] J. E. Jacak, *Explanation of an Unexpected Occurrence of* $\nu = 1/2$ *Fractional Quantum Hall Effect States in Monolayer Graphene*, J. Phys. Condens. Matter **31**, 475601 (2019).

[31] Y. Zeng, J. I. A. Li, S. A. Dietrich, O. M. Ghosh, K. Watanabe, T. Taniguchi, J. Hone, and C. R. Dean, *High-Quality Magnetotransport in Graphene Using the Edge-Free Corbino Geometry*, Phys. Rev. Lett. **122**, 137701 (2019).

[32] T. Chakraborty and P. Pietiläinen, *Fractional Quantum Hall Effect at Half-Filled Landau Level in a Multiple-Layer Electron System*, Phys. Rev. Lett. **59**, 2784 (1987).

[33] X. G. Wen and A. Zee, *Shift and Spin Vector: New Topological Quantum Numbers for the Hall Fluids*, Phys. Rev. Lett. **69**, 953 (1992).

[34] F. D. M. Haldane, *Many-Particle Translational Symmetries of Two-Dimensional Electrons at Rational Landau-Level Filling*, Phys. Rev. Lett. **55**, 2095 (1985).

[35] F. Yang, A. A. Zibrov, R. Bai, T. Taniguchi, K. Watanabe, M. P. Zaletel, and A. F. Young, *Experimental Determination of the Energy per Particle in Partially Filled Landau Levels*, Phys. Rev. Lett. **126**, 156802 (2021).

[36] K. Shizuya, *Electromagnetic Response and Effective Gauge Theory of Graphene in a Magnetic Field*, Phys. Rev. B **75**, 245417 (2007).

[37] I. M. Khalatnikov, *An Introduction to the Theory of Superfluidity* (CRC Press, Cleveland, OH, 2018).

[38] S. M. Girvin, A. H. MacDonald, and P. M. Platzman, *Magneto-Roton Theory of Collective Excitations in the Fractional Quantum Hall Effect*, Phys. Rev. B **33**, 2481 (1986).

[39] E. H. Rezayi, *Reversed-Spin Excitations of the Fractionally Quantized Hall Effect from Finite-Size Calculations*, Phys. Rev. B **36**, 5454 (1987).